Microstructural and metabolic alterations in the zebrafish brain induced by toll-like receptor 2 deficiency: insights from ultra-high field magnetic resonance imaging and spectroscopy

Singer, R.

2

UNVEILING THE EXQUISITE MICROSTRUCTURAL DETAILS AND WHITE MATTER TRACTS IN ADULT ZEBRAFISH BRAIN USING 28.2 T MRI*

*This chapter was published in Molecules 2024; doi:10.3390/molecules29194637

ABSTRACT

Zebrafish is firmly established as an animal model for a wide range of human diseases including neurodegenerative disorders. However, obtaining the microstructural details and studying neuronal network in zebrafish brain non-invasively remains challenging. MRI offers the possibility to non-invasively study zebrafish brain, however due to small brain size, unveiling the exquisite microstructural details from zebrafish brain is difficult. Exploiting higher magnetic fields for imaging can potentially improve the neurological analysis of zebrafish brain as signal-to-noise ratios (SNR) increase with the applied magnetic field strength. Here, we present the first neuroimaging findings of the zebrafish brain at 28.2 T, the highest magnetic field strength currently available for imaging. The performance of MRI at 28.2 T was compared to 17.6 T and an improvement of 20% in SNR was observed at 28.2 T, facilitating the accurate identification of numerous brain substructures. The normative T_1 and T_2 relaxation values were established over different zebrafish brain structures at 28.2 T. To zoom into the white matter structures, we applied diffusion tensor imaging and obtained axial, radial, and mean diffusivity, as well as fractional anisotropy information at a very high spatial resolution. Tractography maps were produced by short-track track-density imaging using the constrained spherical deconvolution method (stTDI CSD). A novel algorithm for stTDI with multi-shell multi-tissue (msmt) CSD was tested on zebrafish brain data, resulting in a significant reduction in false-positive tracks from grey matter compared to stTDI with single-shell single-tissue CSD. This allowed the identification of white matter structures with remarkable resolution and contrast. Our study demonstrates that neuroimaging at 28.2 T provides excellent microstructural details and yields reproducible and quantitative maps of fibre organisation in the intricate zebrafish brain. This work paves the way for future non-invasive studies at ultra-high magnetic field aimed at investigating disease-related microstructural alterations in zebrafish models of various brain diseases.

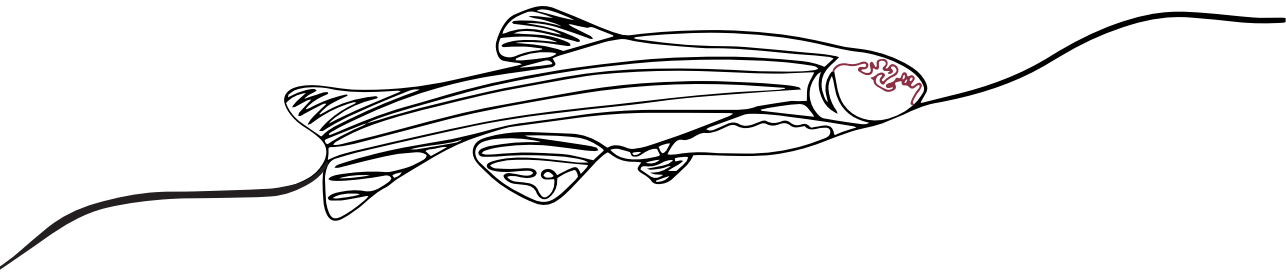

1. INTRODUCTION

Zebrafish (*Danio rerio*) is an excellent animal model in the studies of diseases, biological pathways, genetics, and toxicology[1-4]. In the field of neurodegenerative conditions, zebrafish offer various models including those for Alzheimer's, Parkinson's, and Huntington's disease[5-7]. Therefore, studying the zebrafish brain non-invasively might provide valuable information on the pathology and treatment of neurodegenerative disorders. Magnetic resonance imaging (MRI) is a well-established, non-invasive technique for neuroimaging in both human and animal models. In our previous reports, a successful examination of zebrafish was performed at high field (9.4 T)[8-10] and ultra-high field (17.6 T) MRI[11-13]. High-quality images gave access to anatomical details, allowing visualization of white matter (WM) lesions in zebrafish models of familial cystic leukoencephalopathy[9] and Lowe syndrome[10], as well as *in vivo* analysis of malignant melanoma tumors[13]. Additionally, *in vivo* high-resolution localized magnetic resonance spectroscopy (MRS) was successfully applied to obtain the neurochemical metabolite profile of adult zebrafish. However, obtaining the essential resolution for studying small structures with a high signal-to-noise ratio (SNR) remains challenging.

Insight into the microstructural organisation of the zebrafish brain could be obtained by diffusion-based MRI (dMRI), a powerful, non-invasive technique with high sensitivity for water movement[14]. Cellular structures hinder the microscopic random motion of water, making dMRI unique to study the microstructural organisation of tissue. Diffusion tensor imaging (DTI) is an extended dMRI method providing increased structural information by exploiting anisotropic diffusion effects. Diffusion tensors are calculated from directional differences in the MR signals and used to determine the axial diffusivity ($D_{\parallel}$) from the principal eigenvalue, the radial diffusivity ($D_{\perp}$) from the average of two non-principal eigenvalues, the mean diffusivity (*MD*), and the fractional anisotropy (*FA*), the extent of directional preference. In the brain, anisotropic diffusion effects are most prominent in WM due to the ordered structures of its myelinated axon tracts[14]. Changes in the diffusion anisotropy of WM structures have been reported for many neurodegenerative diseases including Alzheimer's disease, Parkinson's disease, amyotrophic lateral sclerosis (ALS), and Huntington's disease[15-25]. The directionality of WM structures is visualized by directional encoded colour (DEC) *FA* maps, combining *FA* with the directionality of the principal eigenvector. However, *FA* colour maps do not visualize the connectivity of WM tracks, nor does the technique account for crossing or closely passing fibres below the applied MRI resolution. In this regard, DTI tractography offers a solution for visualizing WM tracks. DTI tractography is a distinct processing technique of DTI tensors and the only known non-invasive imaging technique for visualizing WM connectivity in the brain. DTI has been successfully used to probe the changes in brain connectivity during neurogenerative diseases in human subjects[26-32]. Combined with the high spatial resolution required for the neurological analysis of zebrafish, dMRI is very challenging for the zebrafish brain. Consequently, knowledge

of diffusivity and connectivity in the zebrafish brain is limited. Freidlin *et al.*[33] obtained good contrast of the spinal cord in adult zebrafish by DTI, while Ullmann *et al.*[34], presented a DTI study in the zebrafish brain and obtained tractography maps using short-track track density imaging with single-shell single-tissue constrained spherical deconvolution (stTDI ssst-CSD). However, the analysis was performed on isolated brain tissue, rather than intact zebrafish. Additionally, Ullmann *et al.* performed DTI with a single non-zero *b*-value, eliminating the possibility of individually estimating WM, grey matter (GM), and cerebrospinal fluid (CSF) signals, therefore possibly resulting in errors and WM overestimation during tractography[35]. Recently, multi-shell multi-tissue (msmt) CSD algorithms were developed, deconvoluting WM, GM, and CSF responses[35]. By filtering GM- and CSF-like signals strongly present in ssst-CSD, false positive tracks are reduced[36,37]. However, msmt-CSD algorithms have so far not been tested for the zebrafish brain.

Exploiting higher magnetic fields for imaging can potentially improve the neurological analysis of zebrafish brain as SNR increases with the applied magnetic field strength (B_0)[38]. Consequently, increased spatial resolution can be obtained without the need for significant elongation of total acquisition time. In this study, the first MRI results at 28.2 T are presented that were obtained from the zebrafish brain. The performance of MRI at 28.2 T was compared to 17.6 T and a wide range of MR sequences were optimized, including anatomical imaging by rapid acquisition with relaxation enhancement (RARE). Moreover, diffusion-weighted imaging (DWI) was applied to quantify apparent diffusion coefficient (*ADC*) values in several zebrafish brain regions. Furthermore, WM tractography was conducted through DTI using stTDI CSD. Our findings not only include the initial results of stTDI through ssst-CSD on intact zebrafish, but also show the first outcomes of stTDI through msmt-CSD on the zebrafish brain.

2. METHODS

Zebrafish husbandry

The husbandry and use of adult zebrafish described in this study was approved by the local animal welfare committee of the University of Leiden (Licence numbers AVD1060020171767 and AVD10600202216175), following the international guidelines specified by the EU Animal Protection Directive 2010/63/EU, and was conducted according to standard protocols (www.zfin.org) and in compliance with the ARRIVE guidelines as described previously[12,39]. In this study, adult zebrafish (wild-type, male, n = 6) were used. Adult zebrafish aged around 4 months were euthanized through immobilization by submersion in ice water (0 – 4 ˚C) for at least 10 minutes following cessation of opercular movement and then fixed in 4% buffered paraformaldehyde (Zinc Formal-Fixx, ThermoShandon, UK) for 4 days prior to MRI measurements.

Magnetic resonance imaging

MRI was performed using 28.2 T (1.2 GHz) or 17.6 T (750 MHz) vertical bore systems (Bruker Biospin, Ettlingen, Germany). Both systems were equipped with a MICRO 5 gradient system (G_{max} = 3 T/m), a 5 mm birdcage RF coil, and a GREAT 60 gradient power supply. Data acquisition and processing were performed using Paravision 360 v3.3 (Bruker Biospin, Ettlingen, Germany). For all measurements, animals were transferred to 5 mm NMR tubes and embedded in perfluoropolyether (Fomblin Y, Solvay Solexis S.P.A.). To achieve maximal signal intensity, the position of the brain was aligned to the centre of the RF coil. Magnetic field homogeneity was achieved by second-order shimming. A variety of scan protocols was used and optimized for the magnetic field strength of 28.2 T. Identical scan protocols were then used for both MR systems (17.6 T and 28.2 T). For anatomical imaging, a two-dimensional (2D) RARE sequence was employed. Images were acquired with an echo time *TE* = 5.6 ms, a repetition time *TR* = 3000 ms, using 4 segmenting refocusing echoes (RARE factor), and a spatial resolution of 23 × 23 µm. RARE images were obtained with a slice thickness of either 100 µm or 200 µm, with the number of scan being *ns* = 64 or *ns* = 16, respectively, for averaging.

For the estimation of spin-spin relaxation times T_2 a 2D multi-slice multi-echo (MSME) protocol was used, based on the Carr-Purcell-Meiboom-Gill (CPMG) sequence[40]. MSME measurements were performed with 15 echo images per excitation at an echo spacing τ = 5 ms, *TR* = 2500 ms, *ns* = 4, at a spatial resolution of 23 × 23 µm, and with a slice thickness of 200 µm. For estimation of the spin-lattice relaxation times T_1, a 2D RARE protocol at variable repetition times (VTR) was used. Signal intensities were measured at *TR* = 300, 606, 967, 1408, 1974, 2767, 4100, or 10000 ms, *TE* = 3 ms, *ns* = 2, at a spatial resolution of 47 × 47 µm and a slice thickness of 200 µm.

DWI was performed with a 2D diffusion-weighted spin echo sequence with *TE* = 20.2 ms, *TR* = 1000 ms, *ns* = 4, at a spatial resolution of 23 × 23 µm and a slice thickness of 200 µm. MR signals were measured at *b*-values of 75, 500, 1000, 3500, 5000, or 7500 s/mm^2. 2D DTI with echo planar imaging (EPI) was performed at an anisotropic resolution of 25 × 25 µm, at a slice thickness of 200 µm, with *TE* = 12.4 ms, *TR* = 2000 ms, *ns* = 32, and an EPI factor of 8. Multi-shell experiments were performed with *b*-values of 4, 1000, 3500, or 6000 s/mm^2 with 8, 12, 24, or 36 diffusion-encoding directions respectively. Three-dimensional (3D) DTI was performed at an isotropic spatial resolution of 35 µm, with *TE* = 9.1 ms, *TR* = 2000 ms, *ns* = 4, and an EPI factor of 8. Multi-shell experiments were performed with *b*-values of 100, 1000, or 2500 s/mm^2 with 4, 12, or 24 diffusion-encoding directions respectively. Automatic drift compensation was applied to compensate for possible $\mathbf{B}_0$ drift.

Data processing

Identification of brain regions and WM structures was performed based on the adult zebrafish brain atlas[41] and the topological atlas[42].

For the estimation of *SNR*, RARE intensity images were processed in Matlab (mathworks.com). Brain tissue was selected using the volume segmenter tool and the average signal intensity was calculated. For noise, 10 × 10 voxels were selected outside the fish. From these data, *SNR* was calculated using,

$$SNR = \frac{\mu_S - \mu_N}{\sigma_N} \tag{2.1}$$

Here μ_S is the mean intensity of the brain signal, μ_N is the mean intensity of the noise and σ_N is the standard deviation of the noise. SNR maps were created by estimating *SNR* for each voxel inside the RARE intensity image. Signals outside the fish were set to zero by a signal intensity threshold.

For the estimation of T_1, T_2, and *ADC*, nine regions of interest (ROIs) were manually selected in the zebrafish brain using Paravision 360 v3.3. T_1 was estimated by the image sequence analysis tool in Paravision using a non-linear least square algorithm for the mono-exponential fit function

$$I_{TR} = A + I_0 \cdot \left(1 - \exp^{\frac{-TR}{T_1}}\right) \tag{2.2}$$

where I_t is the signal intensity at *TR*, *A* is the absolute bias, and I_0 is the signal intensity at TR_0. From MSME data, T_2 was estimated using the image sequence analysis tool in Paravision with a non-linear least square algorithm for the mono-exponential fit function

$$I_{TE} = A + I_0 \cdot \exp^{\frac{-TE}{T_2}} \tag{2.3}$$

where I_t is the signal intensity at *TE* and I_0 is the signal intensity at TE_0. To reduce the effect of imperfect 180° pulses, uneven echoes were excluded from the data fitting[43]. *ADC* was estimated from DWI data by the image sequence analysis tool in Paravision with a non-linear least square algorithm for the mono-exponential fit function

$$I_b = A + I_0 \cdot \exp^{-b \cdot ADC} \tag{2.4}$$

Here, I_b is the signal intensity at *b* and I_0 is the signal intensity at b_0.

Processing of 2D and 3D DTI data was performed by MRtrix3[44]. Brain masks were manually created using the volume segmenter tool in Matlab. Using MRtrix3 functions, the denoising of DTI data was based on the random matrix theory[45]. Diffusion tensors (**D**) were calculated by fitting the diffusion tensor to the log of the denoised DTI data by minimizing the weighted least-squares and iterated weighted least-squares[46,47]. From the tensors, the $D_{\parallel}$, $D_{\perp}$, *MD*, and *FA* were calculated. *FA* colour maps were generated by adding the directionality of the principal eigenvalue of **D** to *FA* maps. MRtrix3 was used to generate super-resolution (5 µm) stTDI maps from 2D and 3D DTI data. Constrained spherical deconvolution (CSD) was used to resolve crossing fibres by estimating fibre orientation distribution functions (fODFs). Single-shell single-tissue (ssst) CSD response functions were estimated by the Tournier algorithm[48], using the highest *b*-value of the DTI dataset. fODFs were calculated with the ssst-CSD algorithm[49]. Multi-shell multi-tissue (msmt) CSD response functions were estimated by the Dhollander algorithm[36]. Crude segmentation of WM and GM/CSF voxels in 2D and 3D DTI data was performed at *FA* = 0.2. WM, GM, and CSF voxel selection of 3D DTI data for response function estimation was performed with the top 0.5% of refined WM voxels, 2.0% of refined GM voxels, and 10% of refined GM voxels. For the 2D DTI data, 10% of the refined WM voxels were used in the final selection due to the lower total number of available voxels compared to the 3D DTI data set. Finally, msmt-CSD fODFs were calculated with the msmt-CSD algorithm[37]. Whole brain fibre tracking was performed with the iFOD1 algorithm[50]. 1 million (2D DTI data) and 10 million (3D DTI data) tracks were generated with a minimal track length of twice the voxel size and a maximal track length of ten times the voxel size. Fibre generation was automatically terminated once leaving the pre-defined brain mask. Additional parameters were used in their default mode[44]. Tractography results were transformed into super-resolution track density imaging (TDI)[51], resulting in approximately 5µm isotropic resolution. The directionality of generated tracks is visualized by DEC.

3. RESULTS AND DISCUSSION

This study presents the first MRI findings of the zebrafish brain with a state-of-the-art magnetic field strength of 28.2 T. The zebrafish has become a popular species for studying neurological disorders due to the growing understanding of its nervous system and the availability of numerous transgenic zebrafish models[5,6,9,10,13]. Non-invasive MRI methods have significant potential for investigating brain pathology in these models. However, obtaining the essential resolution for studying microstructures and diffusion processes with a high SNR remains challenging for zebrafish brain. In this work, we have optimized and successfully applied MRI methods at 28.2 T magnetic field strength to resolve microstructural details and white matter tracts in the young adult zebrafish brain.

A

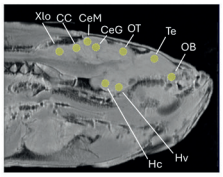

B

	OB	Te	CeG	Xlo	Cem	CC	OT	Hc	Hv
T_1 (ms)									
28.2 T	3000 ± 68	3182 ± 75	2928 ± 60	2942 ± 97	2923 ± 67	2940 ± 88	2812 ± 47	2842 ± 55	2961 ± 56
17.6 T	2746 ± 80	2972 ± 87	2554 ± 17	2638 ± 28	2565 ± 53	2780 ± 34	2539 ± 16	2648 ± 47	2812 ± 38
Factor	1.09	1.07	1.15	1.12	1.14	1.06	1.11	1.07	1.05
T_2 (ms)									
28.2 T	27.8 ± 0.7	26.9 ± 0.9	20.7 ± 0.4	27.2 ± 0.5	27.8 ± 0.5	31.7 ± 1.2	27.5 ± 0.6	28.0 ± 1.0	27.5 ± 2.0
17.6 T	31.3 ± 1.1	29.4 ± 0.4	23.6 ± 1.0	30.0 ± 0.8	30.2 ± 1.4	34.0 ± 0.7	27.7 ± 1.6	33.0 ± 0.6	32.7 ± 1.0
Factor	0.89	0.91	0.88	0.91	0.92	0.93	0.99	0.85	0.84

Figure 2.1. T_1 and T_2 relaxation time measurements in various brain regions of adult zebrafish. [A] *Anatomical RARE image of adult zebrafish indicating the location of ROIs selected for T_1 and T_2 quantification.* ***[B]*** *T_1 and T_2 relaxation time values in various zebrafish brain regions measured at 28.2 and 17.6 T. One-way analysis of variance (ANOVA) with the Bonferroni test for comparison of mean between T_1, T_2 values at two magnetic field was performed and statistically significant difference in both T_1 and T_2 values at two fields was observed ($p < 0.05$). The difference between T_1 and T_2 values measured at two different magnetic field strengths is presented as fold change (Factor). Selected ROIs; Xlo – Vagal lobe; CC – Cerebellar crest; CeM – Cerebellar corpus, molecular layer; CeG – Cerebellar corpus, granular layer; OT – Optic Tectum; Te - Telencephalon; OB – Olfactory bulb; Hc – Caudal zone of periventricular hypothalamus; Hv – Ventral zone of periventricular hypothalamus. Data represent the mean T_1 and T_2 in ms ± standard error (SE) (Error bars); n = 6.*

Relaxation times

The application of MRI at an ultra-high field of 28.2 T requires adjustment of image acquisition parameters, which are based on knowledge of the MR relaxation properties of the tissues being imaged. To establish regional T_1 and T_2 values of the zebrafish brain at 28.2 T, relaxation times were estimated in nine manually selected ROIs (Figure 2.1A); the vagal lobe (Xlo), granular layer of the cerebellar corpus (CeG), telencephalon (Te), olfactory bulb (OB), molecular layer of the cerebellar corpus (Cem), cerebellar crest (CC), optic tectum (OT), caudal zone of the periventricular hypothalamus (Hc), and the ventral zone of the periventricular hypothalamus (Hv). Figure 2.1B shows relaxation times T_1 and T_2 for selected ROIs at 28.2 T and compared them with values obtained at 17.6 T. A clear increase of T_1 and a decrease of T_2 were observed in all selected ROIs at 28.2 T compared to 17.6 T. On average, T_1 increased by a factor of 1.097 ± 0.015, while T_2 decreased by a factor of 0.905 ± 0.011 at 28.2 T compared to 17.6 T. The observed shift in relaxation times at increasing $\mathbf{B}_0$ is consistent with previous reports[52-54]. Generally, T_1 is proportional to $B_0^{1/3}$. Here, all brain regions report a T_1 increase below the theoretical expectations. This is consistent with T_1 reported in mouse brain tissue at 9.4 T and 17.6 T, where an average T_1 increase factor of 1.08 was reported, well below the theoretical increase factor of 1.23[55]. For T_2, the observed decrease at higher magnetic fields is consistent with previous reports as well. In mouse brain regions, increasing the magnetic field from 9.4 T to 17.6 T resulted in an average T_2 decrease by a factor 0.72[56], and changing field from 9.4 T to 11.7 T resulted in an average T_2 decrease by a factor 0.83[53]. Besides $\mathbf{B}_0$, the relaxation times of tissues depend on factors like age, gender, acquisition parameters, and pre-treatment (measuring *in vivo* or fixed)[57]. To minimize the effects of additional factors, measurements at 17.6 T and 28.2 T were performed for the same zebrafish and with identical acquisition

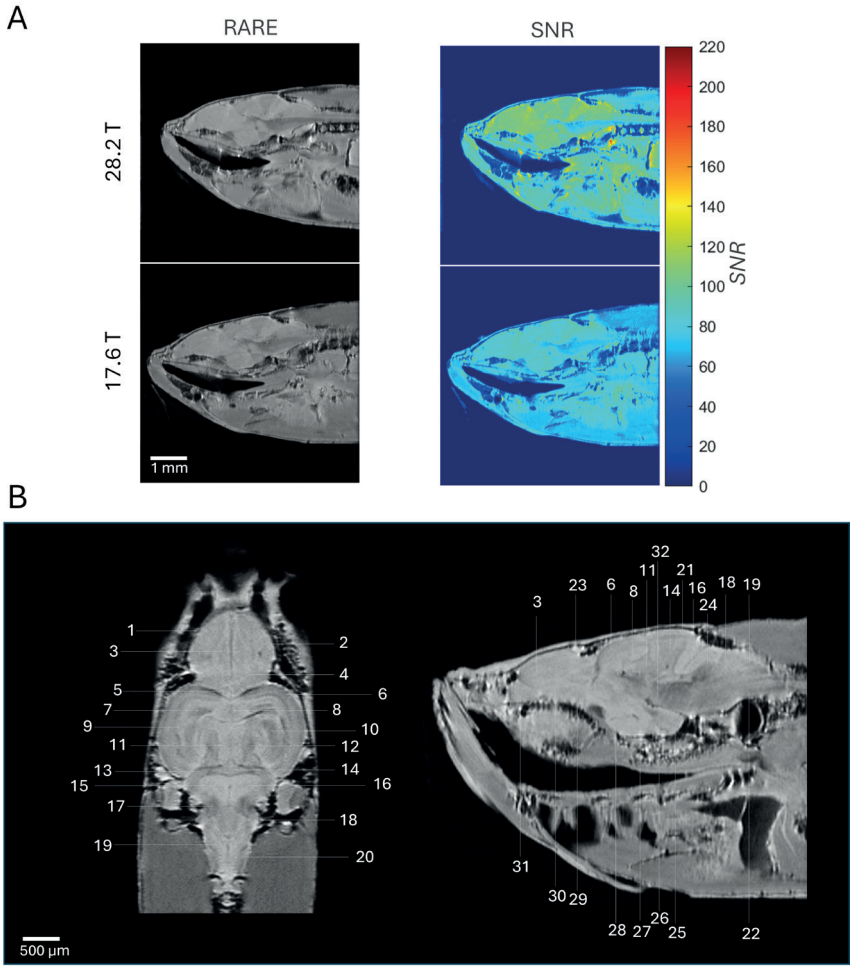

Figure 2.2. Comparison of the anatomical images of the zebrafish brain measured at 17.6 T and 28.2 T. [A] *Representative RARE images (left column) of the zebrafish brain acquired at 17.6 T and 28.2 T. Acquisition details: TR = 3000 ms, TE = 5.6 ms, ns = 16, resolution 23 µm × 23 µm × 200 µm, RARE factor 4. SNR maps generated from RARE images (right column);* ***[B]*** *RARE images of adult zebrafish brain region in coronal (left) and sagittal (right) view acquired at 28.2 T for structure identification. Acquisition details: TR = 3000 s, TE = 5.6 ms, ns = 64, resolution 23 µm × 23 µm × 100 µm, RARE factor 4. Identified structures are as follows: 1 – Central zone of dorsal telencephalon area; 2 – Lateral zone of the dorsal telencephalon; 3 – Medial zone of dorsal telencephalon; 4 – Posterior zone of dorsal telencephalon area; 5 – Dorsal habenular nucleus; 6 – Optic tectum; 7 – Tectal ventricle; 8 – Longitudinal torus; 9 – Periventricular grey zone of optic tectum; 10 – Ventrolateral nucleus of semicircular torus; 11 – Medial division of valvula cerebelli, molecular level; 12 - Medial division of valvula cerebelli, granular layer; 13 – Granular eminence; 14 – Cerebellar corpus, granular layer; 15 – Rhombencephalic ventricle; 16 – Caudal lobe of cerebellum; 17 – Medial octavolateralis nucleus; 18 – Facial lobe; 19 – Vagal lobe; 20 – Medial funicular nucleus; 21 – Cereberal corpus, molecular layer; 22 – Medial longitudinal fascicle; 23 – Dorsal sac, 24 – Cerebellar crest; 25 – Diffuse nucleus of the inferior lobe; 26 – Mammillary body; 27 – Caudal zone of periventricular hypothalamus; 28 – Ventral zone of periventricular hypothalamus; 29 – Parvocellular preoptic nucleus, anterior part; 30 – Ventral nucleus of ventral telencephalon area; 31 – Olfactory bulb; 32 – Interpeduncular nucleus.*

parameters including *TE*, *TR*, RARE factor, number of averages, and acquisition bandwidth. Furthermore, both MR systems contained similar RF coils, gradient power supplies, and software. To summarise, we have established the regional T_1 and T_2 values of the healthy zebrafish brain at 28.2 T. Our findings indicate that T_2 decreases while T_1 continues to rise with increasing magnetic field strength up to the ultra-high 28.2 T level. In future studies, accurate knowledge of T_1 and T_2 values of various brain regions at 28.2 T can serve as a reference point for detecting regional relaxation changes related to diseases in the zebrafish brain.

Anatomical imaging

Figure 2.2A shows representative slices of images of the zebrafish brain acquired using the RARE sequence at 17.6 T and 28.2 T. Images were acquired using the same zebrafish samples and identical acquisition parameters at both magnetic field strengths, obtaining a resolution of 23 µm × 23 µm and a slice thickness of 200 µm. A clear improvement in SNR is observed at 28.2 T as compared to 17.6 T. On average, an SNR improvement factor of 1.2 was found at 28.2 T as compared to 17.6 T in the zebrafish brain. Several brain structures could be clearly identified at 28.2 T (Figure 2.2B). Figure 2.2B shows anatomical images, obtained at 28.2 T, in the coronal and sagittal direction at a field of view (FOV) of 6 × 6 mm, an image size of 256 × 256 voxels, and a slice thickness of 100 µm, resulting in a spatial resolution of 23 × 23 × 100 µm. Excellent contrast, resolution, and SNR allowed for the identification of several brain structures that were verified by comparing them with detailed atlases of the zebrafish brain[41,42].

Diffusion-weighted imaging (DWI)

To get further contrast for the identification of WM structures such as commissures, fibre tracts, nerves, as well as the CSF system, we applied diffusion-based MRI techniques. dMRI provides contrast based on the Brownian motion of water molecules[58]. MRI is made sensitive to diffusion by strong gradient pulses before and after a 180° refocusing pulse, of which the magnitude (G), duration (δ), and time interval (Δ) are summarised in the b-value. In Figure 2.3A, the effect of the applied b-value in DWI experiments is shown for the zebrafish brain. At low b-values of 75 s/mm^2, high contrast and SNR are obtained for all regions in the zebrafish head. At moderate b-values of 500 or 1000 s/mm^2, the signal intensity of muscle and surrounding tissue is reduced, while a high contrast and SNR in the brain are maintained. In fact, DWI images obtained at 1000 s/mm^2 show improved contrast between various brain regions than those obtained at 75 or 500 s/mm^2. This is clearer in the forebrain where the olfactory bulb gained significant contrast compared to anatomical imaging (Figure 2.2B & 2.3A). This allowed better contrast for the identification of various structures in the brain compared to anatomical images obtained by the RARE sequence (Supplementary Figure S2.1). At a high b-values of

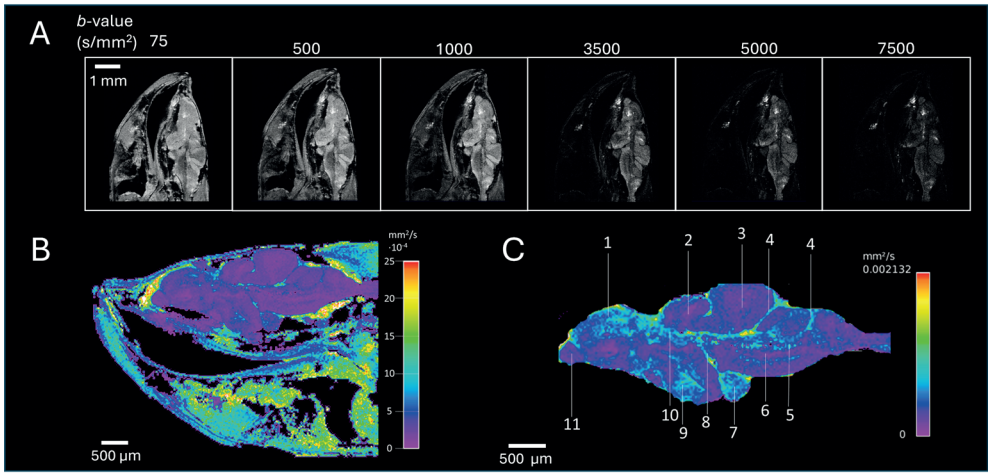

D

	OB	Te	CeG	Xlo	Cem	CC	OT	Hc	Hv
$ADC\left(\cdot 10^{-4}\frac{mm^2}{s}\right)$									
28.2 T	2.9 ± 0.1	4.5 ± 0.4	3.4 ± 0.6	3.9 ± 0.2	3.6 ± 0.3	3.7 ± 0,5	3.6 ± 0.5	3.0 ± 0.4	4.5 ± 0.4
17.6 T	2.4 ± 0.3	5.2 ± 0.4	4.6 ± 0.8	3.9 ± 0.4	4.2 ± 0.7	3.9 ± 0.4	4.5 ± 0.8	3.3 ± 0.2	5.1 ± 0.5
Factor	1.21	0.86	0.74	0.99	0.86	0.96	0.81	0.90	0.89

Figure 2.3. Diffusion-weighted imaging (DWI) of adult zebrafish brain acquired at 28.2 T. [A] *A representative sagittal slice of DWI measurement taken in the head of a zebrafish at increasing b-values. Acquisition details: TR = 1000 ms, TE = 20.2 ms, ns = 4, resolution 23 µm × 23 µm × 200 µm, and effective b-value range 75, 500, 1000, 3500, 5000, or 7500 s/mm²;* ***[B]*** *Apparent diffusion coefficient (ADC) map estimated in brain area of zebrafish, showing high contrast between brain and surrounding tissue;* ***[C]*** *ADC map calculated in brain of zebrafish, demonstrating identification of several structures based on diffusion characteristics; 1 – Medial zone of dorsal telencephalon; 2 – Longitudinal torus; 3 – Cerebellar corpus; 4 – Rhombencephalic ventricle; 5 – Ventral rhombencephalic commisure; 6 – Medial longitudinal fascicle; 7 – Diffusive nucleus of the inferior lobe; 8 – Vasular lacuna of area postrema; 9 – ventral zone of periventricular hypothalamus; 10 – Diencephalic ventricle; 11 – Olfactory bulb;* ***[D]*** *ADC values in various brain regions acquired at 28.2 T and 17.6 T. Data represent the mean ADC (10^{-4} mm² s^{-1}) ± standard error (SE) (Error bars); n = 6.*

3500 s/mm², the MR signal of all tissue drops, although the brain is still visible. Some signal from the brain was even visible at very high *b*-values of 5000 or 7500 s/mm². Figure 2.3B shows the *ADC* map. On average, the brain shows relatively low diffusivity (< 5 mm²/s) compared to most surrounding tissue (> 10 mm²/s), resulting in a clear high contrast between the brain and the surrounding tissue. Figure 2.3C shows an *ADC* map of the brain region from the central imaging slice. In addition to excellent contrast between various brain regions, the CSF system is clearly visible, allowing for the identification of several ventricles. Brain structures including

the diffusive nucleus of the inferior lobe, ventral zone of the periventricular hypothalamus, and medial zone of dorsal telencephalon, show relatively high diffusivity. On the other hand, structures, such as the olfactory bulb, cerebellar corpus, longitudinal torus, and medial longitudinal fascicle show relatively low diffusivity. Figure 2.3D shows estimated *ADC* values for selected ROIs obtained at 17.6 T and 28.2 T (see Figure 2.1A for ROI placement). At both magnetic fields, the highest diffusivity is found in the telencephalon and ventral zone of the periventricular hypothalamus, while the lowest diffusivity is found in the olfactory bulb. Some differences in *ADC* values were seen at 28.2 T as compared to 17.6 T. Although *ADC* values are independent of the applied magnetic field strength, they are affected by SNR. Thus, reported differences at 28.2 T and 17.6 T likely originate from differences in SNR[59].

Diffusion Tensor Imaging

Figure 2.4 shows representative 2D DTI results of adult zebrafish brain obtained at 28.2 T. All images show an identical sagittal slice, rostral (left) to caudal (right), acquired at a resolution of 25 µm x 25 µm, and a slice thickness of 200 µm. Figure 2.4A-C show $D_{\shortparallel}$, $D_{\perp}$, and *MD* maps of the zebrafish brain, respectively. Various structures could be identified by diffusivity-based contrast. The vascular system and specific brain regions, including the telencephalon, diffusive nucleus of the inferior lobe, and the ventral zone of the periventricular hypothalamus show a relatively high diffusivity. However, the olfactory bulb and the optic tectum show relatively low diffusivity compared to other brain structures. These results are consistent with observations made by DWI results shown in Figure 2.3. Furthermore, differences in the $D_{\shortparallel}$ and $D_{\perp}$ are observed, indicating anisotropic diffusivity effects. Figure 2.4D shows the *FA* map, visualizing the extent of anisotropic diffusivity in the zebrafish brain. High *FA* values (light colour) indicate anisotropic diffusion effects, while low *FA* values (dark colour) indicate more isotropic diffusion effects. It is well known that WM structures show the highest *FA* values in the brain due to the ordered structures of its myelinated axon tracts[14]. Due to high *FA* values, WM brain structures show very high image contrast, allowing the identification of various WM structures including the medial longitudinal fascicle, ansulate commissure, posterior commissure, and optic tract (indicated in Figure 2.4D). These structures could not be identified by anatomical imaging or DWI (Figure 2.2 & 3.3). Figure 2.4E shows the DEC *FA* colour map of the central sagittal slice of an adult zebrafish brain, obtained by combining directional information of the principal eigenvalues and *FA* maps. The *FA* colour map further confirms the identification of WM structures by *FA*, showing the rostral-caudal orientation of the medial longitudinal fascicle, and the medial-lateral orientation of the ansulate commissure, posterior commissure, and optic tract.

Figure 2.5A shows representative super-resolution short-track (st) track density imaging (TDI) tractography maps of 2D DTI data. Basic tractography algorithms are deterministic, which allow fitting the diffusion tensors to the diffusion data by tracking paths through the principal eigenvector of the tensor[60]. However, deterministic algorithms do not allow for crossing or closely passing fibres, potentially leading to non-existing connections[61,62]. dMRI tractography with CSD processes crossing and closely passing fibres, based on the first-order integration over fODFs[61]. These fODFs are estimated from response functions, in particular the estimated signal for single-fibre WM. In Figure 2.5A, CSD was performed by ssst algorithms to estimate the response function. The stTDI maps by ssst-CSD show high-resolution fibre-tracts, providing directional information beyond the DTI spatial resolution. Similar stTDI maps have been generated from the zebrafish brain in a previous DTI study performed at a lower magnetic field of 16 T[34]. However, the DTI measurement was accomplished on surgically isolated zebrafish brain treated with an MRI contrast agent. In our work, we performed all the measurements of intact zebrafish at 28.2 T without any contrast agent. One of the shortcomings of performing CSD with ssst-CSD algorithms is that it generates a track map without distinguishing individual

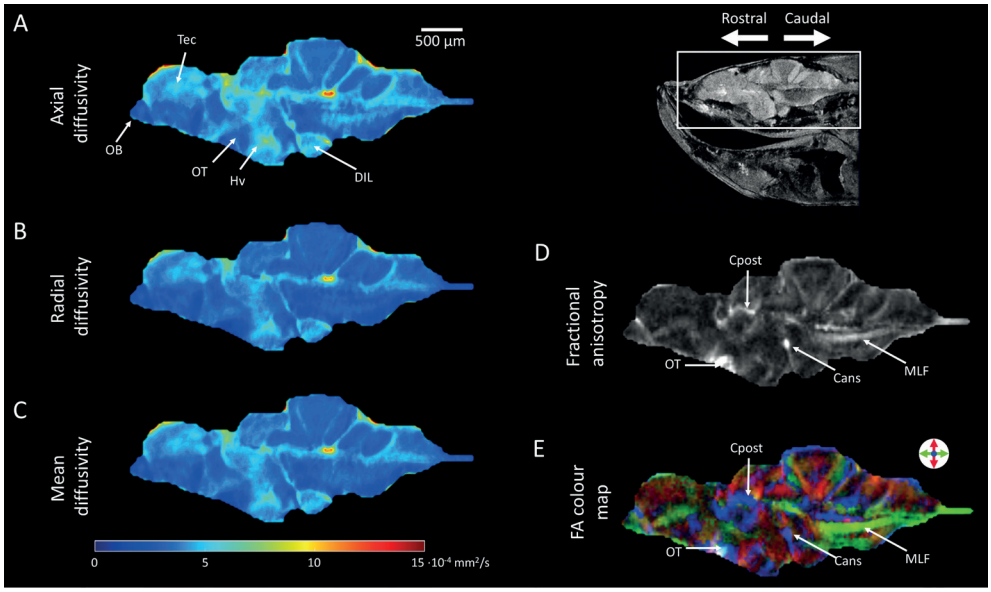

Figure 2.4. White matter structure characterisation based on 2D diffusion tensor imaging (DTI) results of adult zebrafish brain acquired at 28.2 T. *A representative central slice in sagittal view showing colour maps of* ***[A]*** *axial diffusivity ($D_{\parallel}$);* ***[B]*** *radial diffusivity ($D_{\perp}$), and* ***[C]*** *mean diffusivity (MD) calculated from diffusion tensor data.* ***[D]*** *Fractional isotropy (FA); and* ***[E]*** *diffusion-encoded-colour (DEC) map of FA. DEC is used to indicate orientation; green – rostral/caudal, red – dorsal/ventral, and blue – medial/lateral. Abbreviation: MLF – the medial longitudinal fascicle; Cans – ansulate commissure; Cpost – posterior commissure, and OT – optic tract.*

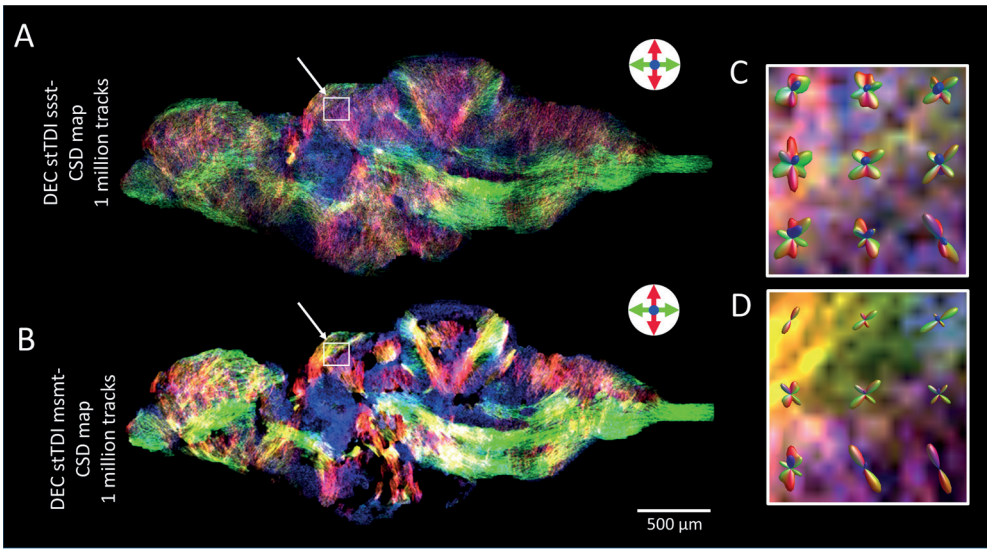

Figure 2.5. Whole brain tractography of zebrafish brain. [A] *Super-resolution DEC stTDI map calculated from single-shell single-tissue (ssst) CSD using the tournier algorithm[48] to estimate the response function.* ***[B]*** *Super-resolution DEC stTDI map calculated from white-matter response function estimated by multi-shell multi-tissue (msmt) CSD using the dHollander algorithm[35]. Tractography performed with one million streamlines, a minimal length of twice the voxel size (50 µm) and a maximum length of ten times the voxel size (250 µm);* ***[C&D]*** *fODFs located in the Optic Tectum isolated from the 2D stTDI ssst-CSD and msmt-CSD map, respectively. The location of these fODFs is highlighted in* ***[A&B]****, respectively. DEC is used to indicate orientation; green – rostral/caudal, red – dorsal/ventral, and blue – medial/lateral.*

anatomical structures, such as GM, CSF, and WM. This potentially produces WM tracking errors and overestimation[35]. To produce tracks exclusively in the WM area, we applied msmt algorithms to obtain stTDI maps (stTDI msmt-CSD). The msmt-CSD was originally developed and optimized for human brain data[37] and has also been applied to mouse brain DTI data[63]. However, it has not yet been applied to the zebrafish brain. In this study we implemented and successfully obtained the stTDI map by msmt-CSD in zebrafish brain (Figure 2.5B).

The response function estimation for WM, GM, and CSF obtained with msmt-CSD derived from our DTI data set is shown in Supplementary Figure S2.2. As can be seen from Figure 2.5B, stTDI by msmt-CSD produced tracks exclusively in WM areas. Furthermore, the stTDI map generated by msmt-CSD demonstrates a significant reduction in noise over those obtained by ssst-CSD (Figure 3.5), leading to improved identification of WM structures. Figure 2.5C&D show fODFs estimated by ssst and msmt CSD algorithms, respectively, from the optic tectum (see the highlighted area in Figure 2.5A&B). As shown in Figure 2.5D, the msmt-CSD fODFs have fewer lobes compared to the ssst-CSD shown in Figure 2.5C. This difference in lobe

number indicates a reduced number of possible tracks obtained by the msmt-CSD method. Our results are consistent with earlier reports in human and mouse brain[37,63]. An increased number of tracks with ssst-CSD indicates tracking errors due to overestimation resulting in false positive WM tracks. Unlike msmt-CSD algorithms, ssst-CSD does not individually characterise WM, GM, and CSF signals, resulting in WM tracking errors and overestimation[35]. The development of the msmt-CSD algorithm revealed that WM, GM, and CSF have distinct dependencies on *b*-values[35], enabling the deconvolution of their individual signals. By filtering GM- and CSF signals, strongly present in ssst-CSD, the number of false positive WM tracks is reduced with the msmt-CSD algorithm[36,37].

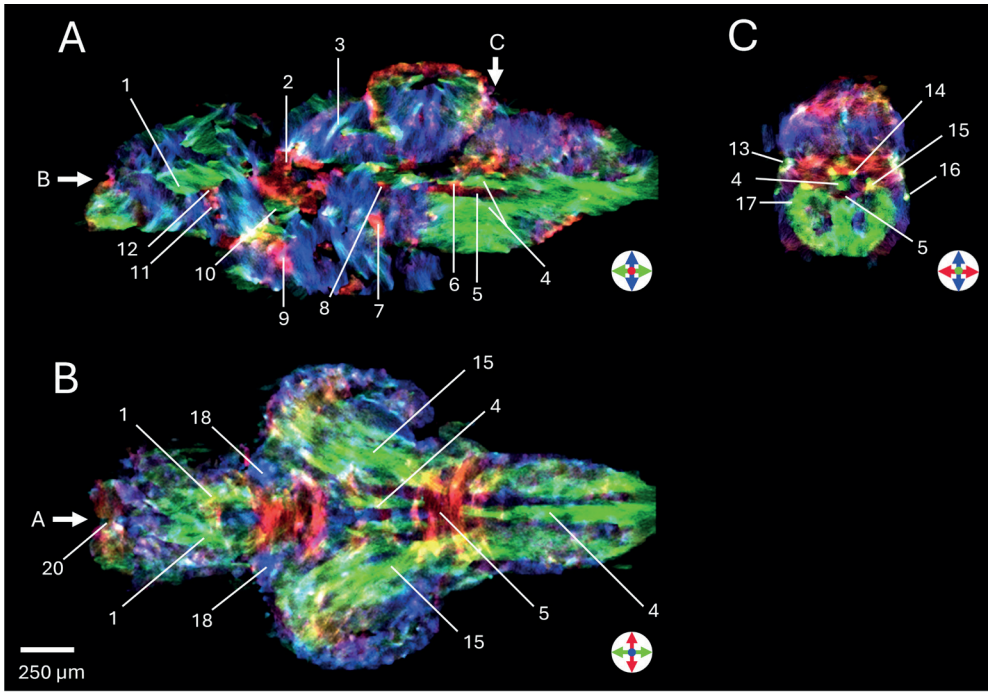

Figure 2.6. 3D super-resolution DEC stTDI msmt-CSD map of adult zebrafish brain. *The DEC stTDI msmt-CSD maps were generated from 3D DTI data measured at 28.2 T. Shown are representative map in* ***[A]*** *sagittal* ***[B]*** *coronal, and* ***[C]*** *axial view. 3D super-resolution DEC stTDI msmt-CSD map allowed identification of several WM structures in zebrafish brain: 1 (MOT) – Medial olfactory tract; 2 (Cpost) – Posterior commissure; 3 (Ctec) – Tectal commissure; 4 (MLF) – Medial longitudinal fascicle; 5 (Cven) – Ventral rhombencephalic commissure; 6 (IAF) – Inner arcuate fibres; 7 (Cans) – Ansulate commissure; 8 (DiV) – Diencephalic ventricle; 9 (Cpop) – Postoptic commissure; 10 (MFB) – Medial forebrain bundle; 11 (CantV) – Anterior commissure; 12 (CantD) – Anterior commissure; 13 (PLLN) - Posterior lateral line nerve; 14 (VIIs) – Sensory root of the facial nerve; 15 (LLF) – Lateral longitudinal fascicle; 16 (ALLN) – Anterior lateral line nerves; 17 (SGT) – Secondary gustatory tract; 18 (DOT) – Dorsomedial optic tract; 19 (Cgus) – Commissure of the secondary gustatory nuclei ; 20 (GL) – Glomerular layer of olfactory bulb. DEC is used to indicate orientation; green – rostral/caudal, blue – dorsal/ventral, and red – medial/lateral.*

Next, we acquire data using 3D DTI, as it allows for better visualization and quantification of white matter tracts, particularly in the areas with complex fibre orientation. The representative 3D DTI results of the adult zebrafish brain, acquired at an isotropic resolution of 35 µm, are shown in Supplementary Figure S2.3. From the 3D DTI data, *FA* maps and DEC *FA* colour maps were generated. Furthermore, 5 µm stTDI tractography maps were created from 3D DTI data (Supplementary Figure S2.3). Both ssst-CSD and msmt-CSD algorithms were used to estimate the response function. Enhanced resolution for crossing and closely passing fibres was clearly obtained with msmt-CSD as compared to ssst-CSD. Similar to 2D DTI data, visualization of WM structures by stTDI with msmt-CSD is significantly improved compared to ssst-CSD.

Figure 2.6 demonstrates the capability to identify WM structures in the zebrafish brain using 3D super-resolution stTDI msmt-CSD. In the sagittal (Figure 2.6A), coronal (Figure 2.6B), and axial (Figure 2.6C) view, WM structures were identified at high contrast and resolution, that were verified by comparing them with detailed atlases of the zebrafish brain[41,42]. A selection of the commissures, fibre tracts, and nerves that could be assigned are shown. This study shows that DTI at ultra-high field in conjunction with stTDI msmt-CSD provide great resolution for visualization of white matter tracts in intact zebrafish without the need to isolate the brain.

4. CONCLUSION

In conclusion, here we have shown the potential of MRI techniques at ultra-high magnetic fields (28.2 T) to study the zebrafish brain non-invasively. Excellent contrast and SNR were obtained allowing for the identification of brain structures, as well as fine white matter structures in intact zebrafish brain. Furthermore, ultra-high field DTI was capable of generating reliable and quantitative representations of the fibre organisation within the small brains of zebrafish. This opens up the possibility to study disease-related changes in white matter structure with super high resolution in a wide range of zebrafish models of human diseases.

ACKNOWLEDGEMENTS

Experiments at the 17.6 T and 28.2 T instruments were supported by the uNMR-NL Grid: A distributed, state-of-the-art Magnetic Resonance facility for the Netherlands (NWO grant 184.032.207). We thank Dr. Julia Krug & Dr. Jeanine Prompers for useful discussions and suggestions. We also acknowledge Dr. Andrei Gurinov for technical support at the uNMR-NL facility and Karthick Babu Sai Sankar Gupta and Fons Lefeber for help at 17.6 T. We would further like to thank Volker Lehmann and Thomas Oerther from Bruker for their help in troubleshooting.

REFERENCES

1 Bailone, R. L. *et al.* "Zebrafish as an animal model for food safety research: trends in the animal research". *Food Biotechnology* **33**, 283-302 (2019). https://doi.org/10.1080/08905436.2019.1673173

2 Cassar, S. *et al.* Use of Zebrafish in Drug Discovery Toxicology. *Chem Res Toxicol* **33**, 95-118 (2020). https://doi.org/10.1021/acs.chemrestox.9b00335

3 Choi, T. Y., Choi, T. I., Lee, Y. R., Choe, S. K. & Kim, C. H. Zebrafish as an animal model for biomedical research. *Exp Mol Med* **53**, 310-317 (2021). https://doi.org/10.1038/s12276-021-00571-5

4 Ding, Y. *et al.* Metabolomic and transcriptomic profiling of adult mice and larval zebrafish leptin mutants reveal a common pattern of changes in metabolites and signaling pathways. *Cell Biosci* **11**, 126 (2021). https://doi.org/10.1186/s13578-021-00642-0

5 Bashirzade, A. A. *et al.* Modeling neurodegenerative disorders in zebrafish. *Neurosci Biobehav Rev* **138**, 104679 (2022). https://doi.org/10.1016/j.neubiorev.2022.104679

6 Wang, X., Zhang, J. B., He, K. J., Wang, F. & Liu, C. F. Advances of Zebrafish in Neurodegenerative Disease: From Models to Drug Discovery. *Front Pharmacol* **12**, 713963 (2021). https://doi.org/10.3389/fphar.2021.713963

7 Wang, J. & Cao, H. Zebrafish and Medaka: Important Animal Models for Human Neurodegenerative Diseases. *Int J Mol Sci* **22** (2021). https://doi.org/10.3390/ijms221910766

8 Kabli, S., Alia, A., Spaink, H. P., Verbeek, F. J. & De Groot, H. J. Magnetic resonance microscopy of the adult zebrafish. *Zebrafish* **3**, 431-439 (2006). https://doi.org/10.1089/zeb.2006.3.431

9 Haud, N. *et al.* rnaset2 mutant zebrafish model familial cystic leukoencephalopathy and reveal a role for RNase T2 in degrading ribosomal RNA. *Proc Natl Acad Sci U S A* **108**, 1099-1103 (2011). https://doi.org/10.1073/pnas.1009811107

10 Ramirez, I. B. *et al.* Impaired neural development in a zebrafish model for Lowe syndrome. *Hum Mol Genet* **21**, 1744-1759 (2012). https://doi.org/10.1093/hmg/ddr608

11 Kabli, S., Spaink, H. P., De Groot, H. J. & Alia, A. In vivo metabolite profile of adult zebrafish brain obtained by high-resolution localized magnetic resonance spectroscopy. *J Magn Reson Imaging* **29**, 275-281 (2009). https://doi.org/10.1002/jmri.21609

12 Eeza, M. N. H. *et al.* Probing microstructural changes in muscles of leptin-deficient zebrafish by non-invasive ex-vivo magnetic resonance microimaging. *PLoS One* **18**, e0284215 (2023). https://doi.org/10.1371/journal.pone.0284215

13 Kabli, S. *et al.* In vivo magnetic resonance imaging to detect malignant melanoma in adult zebrafish. *Zebrafish* **7**, 143-148 (2010). https://doi.org/10.1089/zeb.2009.0649

14 Alexander, A. L., Lee, J. E., Lazar, M. & Field, A. S. Diffusion tensor imaging of the brain. *Neurotherapeutics* **4**, 316-329 (2007). https://doi.org/10.1016/j.nurt.2007.05.011

15 Auning, E. *et al.* White matter integrity and cognition in Parkinson's disease: a cross-sectional study. *BMJ Open* **4**, e003976 (2014). https://doi.org/10.1136/bmjopen-2013-003976

16 Bede, P. *et al.* Patterns of cerebral and cerebellar white matter degeneration in ALS. *J Neurol Neurosurg Psychiatry* **86** (2014).

17 de Schipper, L. J. *et al.* Age- and disease-related cerebral white matter changes in patients with Parkinson's disease. *Neurobiol Aging* **80**, 203-209 (2019). https://doi.org/10.1016/j.neurobiolaging.2019.05.004

18 Gold, B. T., Johnson, N. F., Powell, D. K. & Smith, C. D. White matter integrity and vulnerability to Alzheimer's disease: preliminary findings and future directions. *Biochim Biophys Acta* **1822**, 416-422 (2012). https://doi.org/10.1016/j.bbadis.2011.07.009

19 Huang, P. *et al.* Disrupted white matter integrity in depressed versus non-depressed Parkinson's disease patients: a tract-based spatial statistics study. *J Neurol Sci* **346**, 145-148 (2014). https://doi.org/10.1016/j.jns.2014.08.011

20 Kantarci, K. *et al.* White-matter integrity on DTI and the pathologic staging of Alzheimer's disease. *Neurobiol Aging* **56**, 172-179 (2017). https://doi.org/10.1016/j.neurobiolaging.2017.04.024

21 Novak, M. J. *et al.* White matter integrity in premanifest and early Huntington's disease is related to caudate loss and disease progression. *Cortex* **52**, 98-112 (2014). https://doi.org/10.1016/j.cortex.2013.11.009

22 Reading, S. A. *et al.* Regional white matter change in pre-symptomatic Huntington's disease: a diffusion tensor imaging study. *Psychiatry Res* **140**, 55-62 (2005). https://doi.org/10.1016/j.pscychresns.2005.05.011

23 Stricker, N. H. *et al.* Decreased white matter integrity in late-myelinating fiber pathways in Alzheimer's disease supports retrogenesis. *Neuroimage* **45**, 10-16 (2009). https://doi.org/10.1016/j.neuroimage.2008.11.027

24 van der Burgh, H. K. *et al.* Multimodal longitudinal study of structural brain involvement in amyotrophic lateral sclerosis. *Neurology* **94**, e2592-e2604 (2020). https://doi.org/10.1212/WNL.0000000000009498

25 Zhang, J. *et al.* Regional alterations in cortical thickness and white matter integrity in amyotrophic lateral sclerosis. *J Neurol* **261**, 412-421 (2014). https://doi.org/10.1007/s00415-013-7215-5

26 Abe, O. *et al.* Amyotrophic lateral sclerosis: diffusion tensor tractography and voxel-based analysis. *NMR Biomed* **17**, 411-416 (2004). https://doi.org/10.1002/nbm.907

27 Agosta, F. *et al.* Assessment of white matter tract damage in patients with amyotrophic lateral sclerosis: a diffusion tensor MR imaging tractography study. *AJNR Am J Neuroradiol* **31**, 1457-1461 (2010). https://doi.org/10.3174/ajnr.A2105

28 Kitamura, S. *et al.* Longitudinal white matter changes in Alzheimer's disease: a tractography-based analysis study. *Brain Res* **1515**, 12-18 (2013). https://doi.org/10.1016/j.brainres.2013.03.052

29 Kok, J. G. *et al.* Structural Network Analysis Using Diffusion MRI Tractography in Parkinson's Disease and Correlations With Motor Impairment. *Front Neurol* **11**, 841 (2020). https://doi.org/10.3389/fneur.2020.00841

30 Lo, C. Y. *et al.* Diffusion tensor tractography reveals abnormal topological organization in structural cortical networks in Alzheimer's disease. *J Neurosci* **30**, 16876-16885 (2010). https://doi.org/10.1523/JNEUROSCI.4136-10.2010

31 Phillips, O. *et al.* Tractography of the corpus callosum in Huntington's disease. *PLoS One* **8**, e73280 (2013). https://doi.org/10.1371/journal.pone.0073280

32 Zhang, Y. *et al.* Diffusion tensor imaging of the nigrostriatal fibers in Parkinson's disease. *Mov Disord* **30**, 1229-1236 (2015). https://doi.org/10.1002/mds.26251

33 Freidlin, R. Z. *et al.* Diffusion Tensor MR Microscopy of Adult Zebrafish. *Proc. Intl. Soc. Mag. Reson. Med.* **11** (2004).

34 Ullmann, J. F., Calamante, F., Collin, S. P., Reutens, D. C. & Kurniawan, N. D. Enhanced characterization of the zebrafish brain as revealed by super-resolution track-density imaging. *Brain Struct Funct* **220**, 457-468 (2015). https://doi.org/10.1007/s00429-013-0667-7

35 Dhollander, T., Raffelt, D. & Connelly, A. *Unsupervised 3-tissue response function estimation from single-shell or multi-shell diffusion MR data without a co-registered T1 image*. (2016).

36 Dhollander, T., Raffelt, D., Mito, R. & Connelly, A. Improved white matter response function estimation for 3-tissue constrained spherical deconvolution. *Conference Paper* (2019).

37 Jeurissen, B., Tournier, J. D., Dhollander, T., Connelly, A. & Sijbers, J. Multi-tissue constrained spherical deconvolution for improved analysis of multi-shell diffusion MRI data. *Neuroimage* **103**, 411-426 (2014). https://doi.org/10.1016/j.neuroimage.2014.07.061

38 Krug, J. R. *et al.* Assessing spatial resolution, acquisition time and signal-to-noise ratio for commercial microimaging systems at 14.1, 17.6 and 22.3 T. *J Magn Reson* **316**, 106770 (2020). https://doi.org/10.1016/j.jmr.2020.106770

39 He, J. *et al.* Leptin deficiency affects glucose homeostasis and results in adiposity in zebrafish. *J Endocrinol* **249**, 125-134 (2021). https://doi.org/10.1530/JOE-20-0437

40 Carr, H. Y. & Purcell, E. M. Effects of Diffusion on Free Precession in Nuclear Magnetic Resonance Experiments. *Physical Review* **94**, 630-638 (1954). https://doi.org/10.1103/PhysRev.94.630

41 Kenney, J. W. *et al. A 3D adult zebrafish brain atlas (AZBA) for the digital age*, <http://azba.wayne.edu/> (2021).

42 Wullimann, M. F., Rupp, B. & Reichert, H. *Neuroanatomy of the zebrafish brain A topological atlas*. (1996).

43 Milford, D., Rosbach, N., Bendszus, M. & Heiland, S. Mono-Exponential Fitting in T2-Relaxometry: Relevance of Offset and First Echo. *PLoS One* **10**, e0145255 (2015). https://doi.org/10.1371/journal.pone.0145255

44 Tournier, J. D. *et al.* MRtrix3: A fast, flexible and open software framework for medical image processing and visualisation. *Neuroimage* **202**, 116137 (2019). https://doi.org/10.1016/j.neuroimage.2019.116137

45 Veraart, J., Fieremans, E. & Novikov, D. S. Diffusion MRI noise mapping using random matrix theory. *Magn Reson Med* **76**, 1582-1593 (2016). https://doi.org/10.1002/mrm.26059

46 Basser, P. J., Mattiello, J. & Lebihan, D. Estimation of the Effective Self-Diffusion Tensor from the NMR Spin Echo. *Journal of Magnetic Resonance* **B**, 8 (1994). https://doi.org/https://doi.org/10.1006/jmrb.1994.1037.

47 Veraart, J., Sijbers, J., Sunaert, S., Leemans, A. & Jeurissen, B. Weighted linear least squares estimation of diffusion MRI parameters: strengths, limitations, and pitfalls. *Neuroimage* **81**, 335-346 (2013). https://doi.org/10.1016/j.neuroimage.2013.05.028

48 Tournier, J. D., Calamante, F. & Connelly, A. Determination of the appropriate b value and number of gradient directions for high-angular-resolution diffusion-weighted imaging. *NMR Biomed* **26**, 1775-1786 (2013). https://doi.org/10.1002/nbm.3017

49 Tournier, J. D., Calamante, F. & Connelly, A. Robust determination of the fibre orientation distribution in diffusion MRI: non-negativity constrained super-resolved spherical deconvolution. *Neuroimage* **35**, 1459-1472 (2007). https://doi.org/10.1016/j.neuroimage.2007.02.016

50 Tournier, J. D., Calamante, F. & Connelly, A. MRtrix: Diffusion tractography in crossing fiber regions. *International Journal of Imaging Systems and Technology* **22**, 53-66 (2012). https://doi.org/10.1002/ima.22005

51 Calamante, F., Tournier, J. D., Jackson, G. D. & Connelly, A. Track-density imaging (TDI): super-resolution white matter imaging using whole-brain track-density mapping. *Neuroimage* **53**, 1233-1243 (2010). https://doi.org/10.1016/j.neuroimage.2010.07.024

52 Bottomley, P. A., Foster, T. H., Argersinger, R. E. & Pfeifer, L. M. A review of normal tissue hydrogen NMR relaxation times and relaxation mechanisms from 1-100 MHz: dependence on tissue type, NMR frequency, temperature, species, excision, and age. *Med Phys* **11**, 425-448 (1984). https://doi.org/10.1118/1.595535

53 de Graaf, R. A. *et al.* High magnetic field water and metabolite proton T1 and T2 relaxation in rat brain in vivo. *Magn Reson Med* **56**, 386-394 (2006). https://doi.org/10.1002/mrm.20946

54 Korb, J. P. & Bryant, R. G. Magnetic field dependence of proton spin-lattice relaxation times. *Magn Reson Med* **48**, 21-26 (2002). https://doi.org/10.1002/mrm.10185

55 van de Ven, R. C. *et al.* T(1) relaxation in in vivo mouse brain at ultra-high field. *Magn Reson Med* **58**, 390-395 (2007). https://doi.org/10.1002/mrm.21313

56 Kara, F. *et al.* In vivo measurement of transverse relaxation time in the mouse brain at 17.6 T. *Magn Reson Med* **70**, 985-993 (2013). https://doi.org/10.1002/mrm.24533

57 Hamilton, N., Allen, C. & Reynolds, S. Longitudinal brain studies in adult zebrafish by MRI. (2022). https://doi.org/10.1101/2022.06.09.495545

58 Baliyan, V., Das, C. J., Sharma, R. & Gupta, A. K. Diffusion weighted imaging: Technique and applications. *World J Radiol* **8**, 785-798 (2016). https://doi.org/10.4329/wjr.v8.i9.785

59 Ogura, A. *et al.* Apparent Diffusion Coefficient Value Is Not Dependent on Magnetic Resonance Systems and Field Strength Under Fixed Imaging Parameters in Brain. *J Comput Assist Tomogr* **39**, 760-765 (2015). https://doi.org/10.1097/RCT.0000000000000266

60 Basser, P. J., Pajevic, S., Pierpaoli, C., Duda, J. & Aldroubi, A. In vivo fiber tractography using DT-MRI data. *Magnetic Resonance in Medicine* **44**, 625-632 (2000). https://doi.org/10.1002/1522-2594(200010)44:4<625::Aid-mrm17>3.0.Co;2-o

61 Jeurissen, B., Leemans, A., Jones, D. K., Tournier, J. D. & Sijbers, J. Probabilistic fiber tracking using the residual bootstrap with constrained spherical deconvolution. *Hum Brain Mapp* **32**, 461-479 (2011). https://doi.org/10.1002/hbm.21032

62 Jeurissen, B., Leemans, A., Tournier, J. D., Jones, D. K. & Sijbers, J. Investigating the prevalence of complex fiber configurations in white matter tissue with diffusion magnetic resonance imaging. *Hum Brain Mapp* **34**, 2747-2766 (2013). https://doi.org/10.1002/hbm.22099

63 Jillings, S. *et al.* Multi-tissue constrained spherical deconvolution in a murine brain. *Proc. Intl. Soc. Mag. Reson. Med.* **28** (2020).

5. APPENDIX

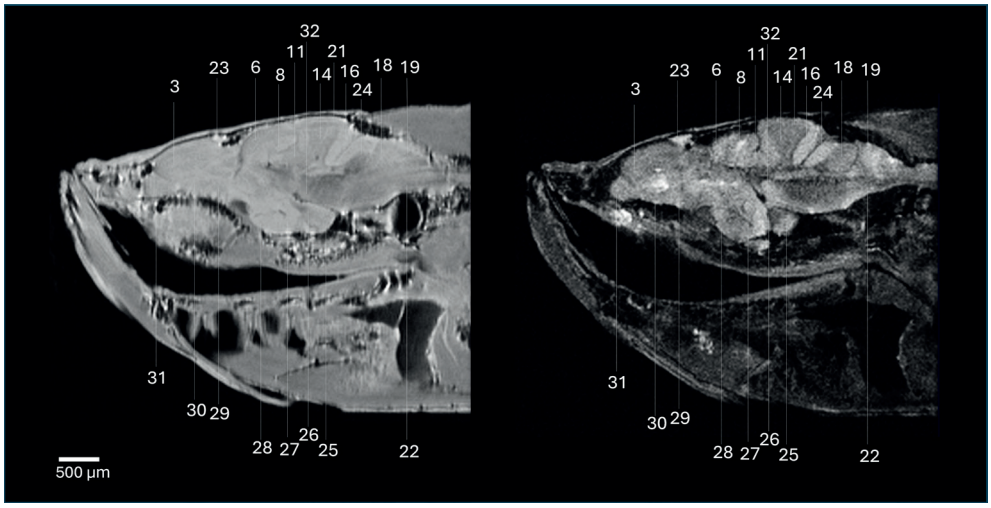

Figure S2.1. Superior identification of brain structures based on diffusion-weighted imaging (DWI) contrast as compared to RARE image contrast. [Left] *A representative sagittal slice of RARE image taken in the head of a zebrafish acquired at 28.2 T. RARE acquisition details: TR = 3000 ms, TE = 5.6 ms, ns = 16, resolution 23 µm × 23 µm × 200 µm, RARE factor 4. SNR maps generated from RARE images (right column);* ***[Right]*** *A representative sagittal slice of DWI measurement taken in the head of a zebrafish at a b-values of 1000 s/mm2. Acquisition details: TR = 1000 ms, TE = 20.2 ms, ns = 4, resolution 23 µm × 23 µm × 200 µm. Structure numbering (kept same as in Figure 3.2): 3 – Medial zone of dorsal telencephalon; 4 – Posterior zone of dorsal telencephalon area; 5 – Dorsal habenular nucleus; 6 – Optic tectum; 7 – Tectal ventricle; 8 – Longitudinal torus; 9 – Periventricular grey zone of optic tectum; 10 – Ventrolateral nucleus of semicircular torus; 11 – Medial division of valvula cerebelli, molecular level; 12 - Medial division of valvula cerebelli, granular layer; 13 – Granular eminence; 14 – Cerebellar corpus, granular layer; 15 – Rhombencephalic ventricle; 16 – Caudal lobe of cerebellum; 17 – Medial octavolateralis nucleus; 18 – Facial lobe; 19 – Vagal lobe; 20 – Medial funicular nucleus; 21 – Cereberal corpus, molecular layer; 22 – Medial longitudinal fascicle; 23 – Dorsal sac, 24 – Cerebellar crest; 25 – Diffuse nucleus of the inferior lobe; 26 – Mammillary body; 27 – Caudal zone of periventricular hypothalamus; 28 – Ventral zone of periventricular hypothalamus; 29 – Parvocellular preoptic nucleus, anterior part; 30 – Ventral nucleus of ventral telencephalon area; 31 – Olfactory bulb; 32 – Interpeduncular nucleus.*

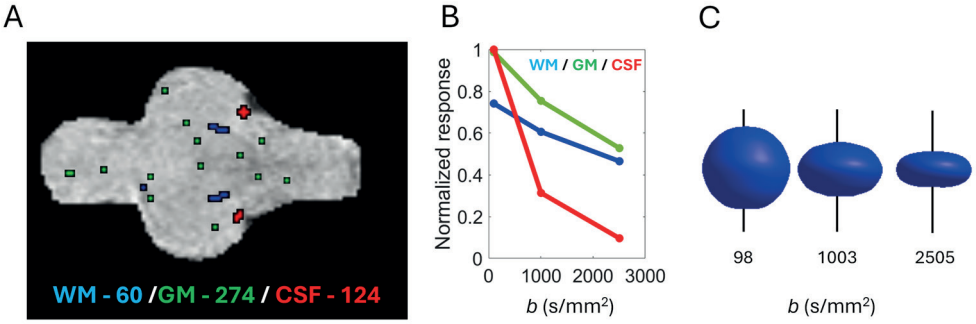

Figure S2.2. Response function estimation from DTI dataset of adult zebrafish brain. [A] *Voxels used for the estimation of response function; WM (blue), GM (green), and CSF (red). The total number of voxels selected for the response function estimation was 60 (WM), 274 (GM), and 124 (CSF).* ***[B]*** *Average normalized tissue response for WM, GM, and CSD as a function of b-values,* ***[C]*** *average angular WM response at applied b-values.*

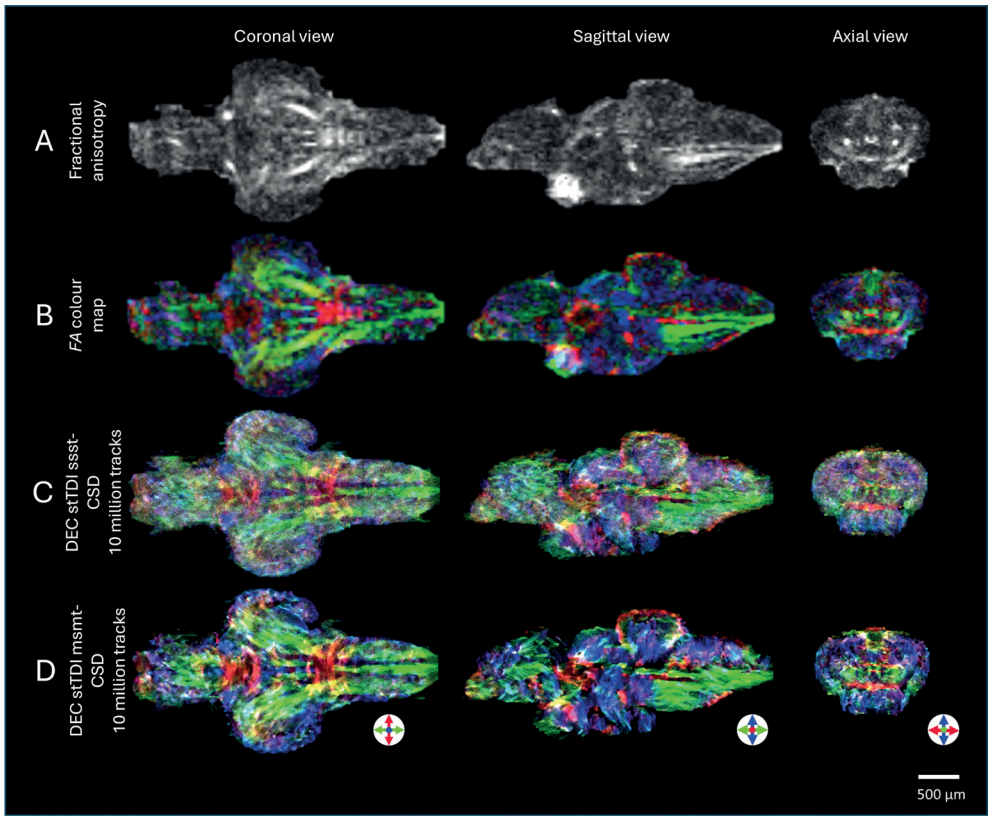

Figure S2.3. 3D DTI results of adult zebrafish brain, showing coronal, sagittal, and axial slices, acquired at 28.2 T. *Diffusion tensors were used to calculate* ***[A]*** *the fractional anisotropy and* ***[B]*** *FA colour map. Short track (st) tractography with Constrained Spherical Deconvolution (CSD) was applied, comparing two different algorithms for the estimation of the response function.* ***[C]*** *Super-resolution DEC stTDI maps calculated from single-shell single-tissue (ssst) CSD using the tournier algorithm (Tournier et al., 2004) [48] to estimate the response function.* ***[D]*** *Super-resolution DEC stTDI map calculated from white-matter response function which was estimated by multi-shell multi-tissue (msmt) CSD using the dHollander algorithm [35]. Tractography performed by generating ten million streamlines, with a minimal length of twice the voxel size (70 µm) and a maximum length of ten times the voxel size (350 µm). DEC is used to indicate orientation; green – rostral/caudal, blue – dorsal/ventral, and red – medial/lateral. Acquisition details: TR = 2000 ms, TE = 9 ms, ns = 4, isotropic resolution 35 µm, effective b-value range 100, 1000, or 2500 s/mm2, with 4, 12 or 24 diffusion-encoding directions respectively.*